Chemical Engineering Journal 526 (2025) 171092

Contents lists available at ScienceDirect

Chemical Engineering Journal

journal homepage: www.elsevier.com/locate/cej

Analyzing the transmembrane and intracellular delivery dynamics and mechanisms of RNA nanoparticles

Hui Wang [a], Xin Ji [b], Haijiao Xu [b], Siying Li [a], Hongda Wang [b,*], Yuping Shan [a,*]

[a] College of Chemistry and Life Sciences, Advanced Institute of Materials Science, Changchun University of Technology, Changchun, 130012, China
[b] State Key Laboratory of Electroanalytical Chemistry, Changchun Institute of Applied Chemistry, Chinese Academy of Sciences, Changchun, 130022, China

ARTICLE INFO

Keywords:
RNA nanoparticles
Transmembrane transporting
Intracellular delivery
Force tracing
Single particle fluorescence tracking

ABSTRACT

RNA nanoparticles (RNA NPs) have emerged as a promising class of nano-drugs with unique advantages and broad application. The RNA NPs with diverse structures and functions can be constructed based on the self-assembly properties of RNA sequences, enabling target specific diseases and cells. However, effective delivery of RNA NPs to targeted cells or tissues remains challenging, understanding their cellular delivery mechanism is crucial for developing efficient delivery systems. The representative three-way junction (3WJ) and four-way junction (4WJ) RNA NPs have been extensively applied as scaffold to construct nano-drugs for targeted delivery. Discovering the cellular delivery dynamics and mechanisms of 3WJ-RNA NPs and 4WJ-RNA NPs could guide the development of optimal delivery systems for RNA NPs therapeutics. Herein, we tracked the transmembrane and intracellular transporting dynamic process of RNA NPs, it is found that the 4WJ-RNA NPs exhibit higher transmembrane transporting efficiency and faster intracellular transporting speed with directed diffusion mode. The detailed intracellular transport pathway of RNA NPs was identified: the RNA NPs is more likely to transport with microtubules rather than actin filaments, and arrive lysosomes preferentially via multivesicular bodies rather than late endosomes. Endosomal escape of RNA NPs was observed from both early endosomes and lysosomes, and more often from lysosomes, 4WJ-RNA NPs escape from lysosomes with higher efficiency. Our results provide valuable insights into the cellular delivery mechanisms of RNA NPs and offer important design considerations for enhancing their therapeutic efficiency.

1. Introduction

The RNA nanotechnology has emerged as a prominent field for biomedical applications, suggesting its potential application in new generation of drug [1,2]. RNA NPs provide an excellent platform for combining therapeutic, targeting, and detection module, all in one nanoparticle [1]. In recent years, RNA NP drugs have gained significant attention in anticancer treatment and vaccine field, particularly following the FDA approval of RNA-based therapeutics and authorization of mRNA COVID-19 vaccines [3]. The pRNA platform has demonstrated the potential for precision delivery of siRNA to cancer receptor targets in breast cancer, cervical cancer, and ovarian cancer [4,5]. As presentative RNA NPs, both 3WJ-RNA NPs and 4WJ-RNA NPs have been shown to enable construction of RNA nano-drugs with high thermodynamic stability [6–9]. Meanwhile, the multiway junction RNA NPs are able to deform their shape to penetrate tiny holes in leaky tumor vasculature, thereby enhancing the permeability and retention (EPR) effect [10]. The 3WJ-RNA NPs have been utilized as a scaffold for fabricating multifunctional and thermodynamically stable nano-drugs with medical potential [11]. It has been demonstrated the advantage of 4WJ-RNA NPs in thermostability, drug payload, and organ accumulation, which enhance therapeutic efficacy [12]. However, whether 3WJ-RNA NPs or 4WJ-RNA NPs need to enter cells and escape from endosomes to exert their effects. An efficient cellular delivery system is crucial for ensuring RNA NP drug therapeutic efficacy and safety, which plays an important role in protecting RNA structure, enhancing targeting ability, reducing drug doses, and minimizing side effects [13]. Comprehensively understanding the cellular delivery mechanisms of RNA NPs can ultimately facilitate the challenging task of predicting RNA nano-drug delivery efficiency.

Herein, the transmembrane transporting dynamic parameters of 3WJ-RNA NPs and 4WJ-RNA NPs were analyzed at single particle level using atomic force microscope (AFM)-based force tracing technique with high temporospatial resolution, which enables detecting of force

* Corresponding authors.
E-mail addresses: hdwang@ciac.ac.cn (H. Wang), shanyp@ccut.edu.cn (Y. Shan).

https://doi.org/10.1016/j.cej.2025.171092
Received 17 March 2025; Received in revised form 28 September 2025; Accepted 19 November 2025
Available online 24 November 2025
1385-8947/© 2025 Elsevier B.V. All rights are reserved, including those for text and data mining, AI training, and similar technologies.

even at 10 pN and capturing ultrafast events down to 10 μs during the cellular uptake [14]. Based on the single particle fluorescence tracking technique, the intracellular delivery fate and efficiency of the RNA NPs were elucidated by analyzing the two-dimensional trajectory and the mean squared displacement (MSD), and the diffusion mode in different endosomes was classified. Meanwhile, the endosomal escape pathway and efficiency of the RNA NPs were evaluated. These findings will facilitate optimizing the RNA NPs delivery system, and provide unique insights for design and development of intelligent diagnosis and therapy RNA nano-drugs.

2. Materials and methods

2.1. Materials

The Human cervical cancer cells (HeLa) and African green monkey kidney cells (Vero) were purchased from the Institutes of Biological Sciences (Shanghai, China). Diethylpyrocarbonate (DEPC) treated water was purchased from Ding Guo. The 3WJ-RNA NPs and 4WJ-RNA NPs were constructed and provided by ExonanoRNA LLC. The sequences of 3WJ-RNA NP and 4WJ-RNA NP are showing as (lower cases letters indicate 2′-F modified nucleotides):

3WJ-A: 5′ uuG ccA uGu GuA uGu GGG (folate) 3′; 3WJ-B: 5′ ccc AcA uAc uuu Guu GAu cc (Cy3) 3′; 3WJC: 5′ GGA ucA Auc AuG GcA A (SH) 3′.

4WJ-A: 5′ uuA GGu AAA Gcc Acc uGc AGG uGc uAc cGA uGu AAu ucA A (Cy3) 3′; 4WJ-B: 5′ uuG AAu uAc Auc GGu AGc AcG GGc uGu GcG AGG cuG AAc AG (SH) 3′; 4WJ-C: 5′ cuG uuc AGc cuc GcA cAG ccA GcA cGc Acc uGA AuA GG 3′; 4WJ-D: 5′ ccu Auu cAG GuG cGu Gcu GGG cuG cAG GuG Gcu uuA ccu AA (folate) 3′.

2.2. Cell culture

HeLa cells and Vero cells were maintained in Dulbecco's modified Eagle's medium (DMEM, BI) containing 10 % fetal bovine serum (FBS, Bioind), 100 μL/mL streptomycin number (Bioind), and 100 μL/mL penicillin antibiotics (Bioind) at 37 °C in humidified environment containing 5 % CO_2. The cells were cultured for 24–48 h until 75 % of the Petri dish was covered with cells [15]. Subsequently, the cells were washed with phosphate-buffered saline (PBS, pH 7.4) three times and serum-free medium (SFM) once in sequence to effectively remove cell debris and unattached cells before use.

2.3. AFM tip modification

The RNA NPs were attached onto the AFM tip (MSCT, D, Bruker, USA) using the reported method [16]. Primarily, the AFM tip was cleaned with the piranha solution (H_2SO_4: 30 % H_2O_2, 3:1, *v*/v) for 20 min, and then treated with ozone for 20 min. After cleaning, they were functionalized with 50 μL of 3-aminopropyltriethoxysilane (APTES) and 20 μL of N, N-diisopropylethylamine (DIPEA) in a desiccator for 10 h by a vapor deposition method. Subsequently, the PEG linker (MAL-PEG_{45}-NHS, MW ~ 2000, 1 mg/mL) was attached to the silylated AFM tips in the presence of triethylamine and trichloromethane (2 h). Then the PEG-modified AFM tips were immersed in a 200 μL solution containing RNA NPs (20 nM) for 2 h. After functionalization, the AFM tips were washed with DEPC-treated water three times and stored in DEPC-treated water at 4 °C protected from light until use.

2.4. Force tracing measurements

Force tracing experiments were carried out with an AFM 5500 system in serum-free culture medium (SFM) at 37 °C controlled by a Model 325 temperature controller (Agilent Technologies, Chandler, AZ). The spring constant of the AFM tip cantilever (MSCT, D-tip) was calibrated by using the thermal noise method [17]. The measurement of force-time curves (~4000) was obtained on at least 20 cells for each data set and collected by a 16-bit DA/AD card (PCI-6361e, National Instruments) controlled by LabVIEW (National Instruments Inc., Austin, Texas, USA). The sampling rate of the data acquisition is 2 MS s^{-1}, and a 100 Hz low-pass filter was used to eliminate high-frequency noise in electronic equipment and the environment. The displacement H of RNA NPs during internalization is equal to the sum of the bending distance d of the AFM tip cantilever and the stretching length h of the PEG linker [17,18]:

$$H = d + h \tag{1}$$

The extended worm-like chain (WLC) model can be used to properly calculate the stretching length h of the PEG linker; the equation used for the calculation is as follows [19]:

$$\frac{FL_P}{K_BT} = \frac{1}{4}\left(1 - \frac{h}{L_0} + \frac{F}{K_0}\right)^{-2} - \frac{1}{4} + \frac{h}{L_0} - \frac{F}{K_0} \tag{2}$$

where Lp represents the persistence length, which is 3.8 Å, K_B stands for the Boltzmann constant, T is the absolute temperature, L_0 is the contour length, h represents the extension length of the PEG linker, K_0 is the enthalpic correction, which is 1561 ± 33 pN, the length of the PEG unit is 4.2 Å, and the total estimated contour length L_0 for PEG is nearly 196 Å. The bending distance of the AFM tip cantilever can be calculated by Hooke's law as follows [20]:

$$F = k \times d \tag{3}$$

where F is the transmembrane force for RNA NP detected from the force-time curves, and k represents the effective spring constant of the AFM tip cantilever. Therefore, the displacement H could be obtained from the above formulas (2)–(4). The duration t of RNA NPs entry into the cells can be obtained from the force-time curves, and the speed v could be calculated as follows [21,22]:

$$v = \frac{H}{t} \tag{4}$$

2.5. SMFS (single molecule force spectroscopy) measurements

The measurements were performed using the same AFM as mentioned above. Force-distance curves were obtained using the contact mode in SFM at 37 °C. The AFM tip cantilever retraction velocity can be determined by changing the scan size and sweep time [23]. The RNA NPs were connected on AFM tip using the same method as mentioned in force tracing experiments.

2.6. Blocking experiments

To inhibit specific endocytic pathway of RNA NPs cellular uptake, we cocultured the inhibitors namely EIPA (10 mM), nystatin (20 μM, Sigma-Aldrich), CPZ (10 μM Sigma-Aldrich), and free folic acid (10 μM, Sigma-Aldrich) with HeLa cells for 30 min at 37 °C, respectively. Before performing force tracing experiments, the cells were washed with PBS and SFM. For fluorescence imaging experiments, the cells were treated under the same conditions as those mentioned above and then cocultured with RNA NPs (100 nM, 2 h). To block microtubule cotransport, HeLa cells expressed GFP-Tub were incubated with nocodazole (30 μM, Sigma-Aldrich) or monastrol (30 μM, MCE) for 30 min, washed three times with PBS, and then incubated with RNA NPs (100 nM) for 45 min at 37 °C. To disrupt actin filaments, HeLa cells expressed LifeAct-staygold were incubated with cytochalasin D (5 μM, Yeasen Biotechnology) for 30 min, washed three times with PBS, and then incubated with RNA NPs (100 nM) for 45 min at 37 °C.

2.7. Fluorescence labeling of cells

Before labeling, the cells were incubated with RNA NPs (100 nM) for 2 h at 37 °C, and then the cells were fixed with 4 % paraformaldehyde

(PFA) for 30 min and washed three times with PBS. Subsequently, the cells were incubated with the Hoechst 33342 (Biyuntian; 1:1000 dilution) for 10 min and WGA-ALexa-Fluor^{647} (Thermo Fisher Scientific; 1:1000 dilution) for 10 min to label the nucleus and membrane, respectively.

2.8. Cell transfection

The cells were transiently transfected with plasmids using the transfection reagent Lipofectamine 3000 (Invitrogen) according to the manufacturer's instructions. In brief, 1 to 2 μg plasmid and 2 to 4 μg transfection reagent were mixed in Opti-MEM medium (Gibco, Thermo Fisher Scientific) and then incubated with cells. HeLa cells were transiently transfected with the plasmid GFP-Clathrin (Sino Biological), GFP-Tub (Crisprbio), LifeAct-staygold, GFP-Rab5, GFP-Rab7, GFP-Rab11, GFP-CD63 and GFP-Lamp (Sino Biological), respectively. The cells were subsequently cultured for the indicated time before imaging or other analysis.

2.9. Confocal microscopy fluorescence imaging

Confocal and time-lapse imaging were collected using a 100×/1.49 oil objective on a Nikon Eclipse Ti inverted microscope equipped with an Andor (Oxford Instruments) spinning disk confocal imaging system, a Yokogawa CSU-X1, and an Andor iXon Ultra electron-multiplying charge-coupled device (EMCCD) camera [24]. The Hoechst 33342 was excited with a 405 nm laser. GFP-Clathrin, GFP-Tub, LifeAct-staygold, GFP-Rab5, GFP-Rab7, GFP-Rab11, GFP-CD63 and GFP-Lamp were excited with a 488 nm laser. Cy3 were excited with a 561 nm laser. WGA-ALexa-Fluor^{647} was excited with a 640 nm laser. Images were captured at 37 °C and supplied 5 % CO_2 by an incubation chamber (Tokai Hit Co., Ltd.). For time-lapse tracking, serial images were recorded at a high frequency with the iXon Ultra EMCCD instrument. The microscope objective is equipped with a piezo-actuator for fast, precise, automated closed-loop focal plane control (PRIOR). For 3D volume reconstruction, one image stack was acquired using the precise motorized stage with approximately 50–70 z-axis slices an axial distance of 0.2 μm between two images. Then, XY, XZ, and YZ sections were imaged. Finally, 3D images were acquired by reconstructing maximum z projections of XY sections. The above images were acquired and processed with Andor iQ3 imaging software. The data are representative of at least three independent experiments with approximately 50 cells each.

2.10. CCK-8 viability assay

HeLa cells were seeded in a 96 well plate with the density of 5×10^3 cells/well and cultured for 24 h. After washing the cells three times with PBS, 100 μL of fresh medium containing different inhibitors (EIPA 10 mM, nystatin 20 μM, CPZ 10 μM, nocodazole 30 μM, monastrol 30 μM and cytochalasin D 5 μM) was added into per well, respectively. After culturing for 30 min, 10 μL CCK-8 (APE-Bio) was added to each well, and the cells were incubated further for 1 h. The optical density (OD) of the cell suspensions at 450 nm was measured using a microplate reader (Bio-Rad, USA). The cell viability was calculated as $(OD_{sample} - OD_{blank}) / (OD_{control} - OD_{blank}) \times 100$ %.

2.11. DLS measurement

The RNA NPs was incubated in a buffer containing 25 mM citrate-phosphate, 2 mM DTT and 0.5 U/mL cathepsin B, followed by measurement of the apparent hydrodynamic diameter of RNA NPs using the Malvern Zetasizer (Malvern Instrument). Three independent experiments were conducted, and the average size of RNA NPs was obtained.

2.12. Data analysis

The fluorescent images were processed with ImageJ software, including fluorescent signal extraction, colocalization recognition, and trajectory reconstruction. The MSD of the RNA NPs was calculated using Origin software. The motion mode was distinguished by fitting the MSD and change in time (Δt) to different functions as follows [25,26]:

$$\mathrm{MSD}(\Delta t) = 4D\Delta t + \mathrm{V}^2(\Delta t)^2 \text{ (directed diffusion mode)} \quad (5)$$

$$\mathrm{MSD} = 4D\Delta t \text{ (simple diffusion mode)} \quad (6)$$

$$\mathrm{MSD} = 4D\Delta t^{\alpha} \text{ (restricted diffusion mode)} \quad (7)$$

3. Results and discussion

3.1. Capturing the transmembrane behavior of single 3WJ-RNA NP and 4WJ-RNA NP

To study the transmembrane and intracellular delivery of RNA NPs, two representative RNA NPs, the 3WJ-RNA NPs (5 nm in diameter) and 4WJ-RNA NPs (10 nm in diameter) were selected (purchased from ExonanoRNA), and the structure has been visualized by AFM imaging previously [27]. The end of 3WJ-A strand 3′, 3WJ-B strand 3′, and 3WJ-C strand 3′ was modified with folate (FA), fluorochrome (Cy3), and sulfhydryl (-SH), respectively. The end of 4WJ-A strand 3′, 4WJ-B strand 3′, and 4WJ-D strand 3′ were modified with Cy3, -SH, and FA, respectively (Fig. S1a, b). The serum stability of the RNA NPs has been verified in previous report [28,29]. The confocal laser scanning microscope (CLSM) imaging results indicate that both 3WJ-RNA NPs and 4WJ-RNA NPs are internalized. The magnified images of the XY plane and XZ, YZ cross-sectional planes show that the RNA NPs is really located inside the cytoplasm around the nucleus (Fig. S2a, b). With prolonging incubation time (15, 30, 60, and 120 min), the more and more RNA NPs is observed in the cytoplasm (Fig. 1a). The average fluorescence number in each cell for 4WJ-RNA NPs (15 ± 6, 24 ± 7, 30 ± 6, and 41 ± 10 at 15, 30, 60, and 120 min, respectively) is obviously larger than that for 3WJ-RNA NPs (5 ± 2, 8 ± 3, 11 ± 4, and 16 ± 4 at 15, 30, 60, and 120 min, respectively) at each incubating time (Fig. 1b, c), which can be attributed to the higher transmembrane transporting ability of 4WJ-RNA NPs.

The transmembrane transport ability of 3WJ-RNA NP and 4WJ-RNA NP was further evaluated by monitoring the single particle transmembrane process based on force tracing technique. The RNA NPs was covalently bound to the AFM tip via heterobifunctional polyethylene glycol (MAL-PEG$_{45}$-NHS, MW: 2000) linker, where the NHS group is used to immobilize on the aminated AFM tip, and the MAL group reacts with the -SH on the RNA NPs (Fig. 1d). Prior to conducting force tracing experiments, the RNA NPs modified AFM tip is positioned above the relatively flat region of cell periphery with the assistance of a CCD camera (Fig. S3a). The contact point between RNA NPs and the cell membrane is determined by measuring the force-distance curves (Fig. S3b). Subsequently, the RNA NP-functionalized AFM tip is moved to the contact point, slightly contacting cell membrane without driving force from AFM setup, finally closes the feedback system. Once the FA on RNA NPs was recognized by the folate receptor (FR) on cell membrane (I), the spontaneous cellular uptake of RNA NP will stretch the PEG linker and further induce the bending downwards of the AFM tip cantilever (II, Fig. 1e, f). The deflection will be recorded with time going and converted into a force-time curve. Then, the piezoelectric ceramic drives the AFM tip cantilever to maintain a balanced position, and the force-time curve returns to flat due to the principle of the force tracing in constant position mode (Fig. S4a). The typical force-time curves (Fig. 1g) exhibit the distance from the start point to the end point in horizontal and vertical direction, representing the required time and force for single RNA NP transmembrane respectively. The force ranges from 20 to 61 pN with the mean value of 35 ± 9 pN and 33 ± 8 pN for

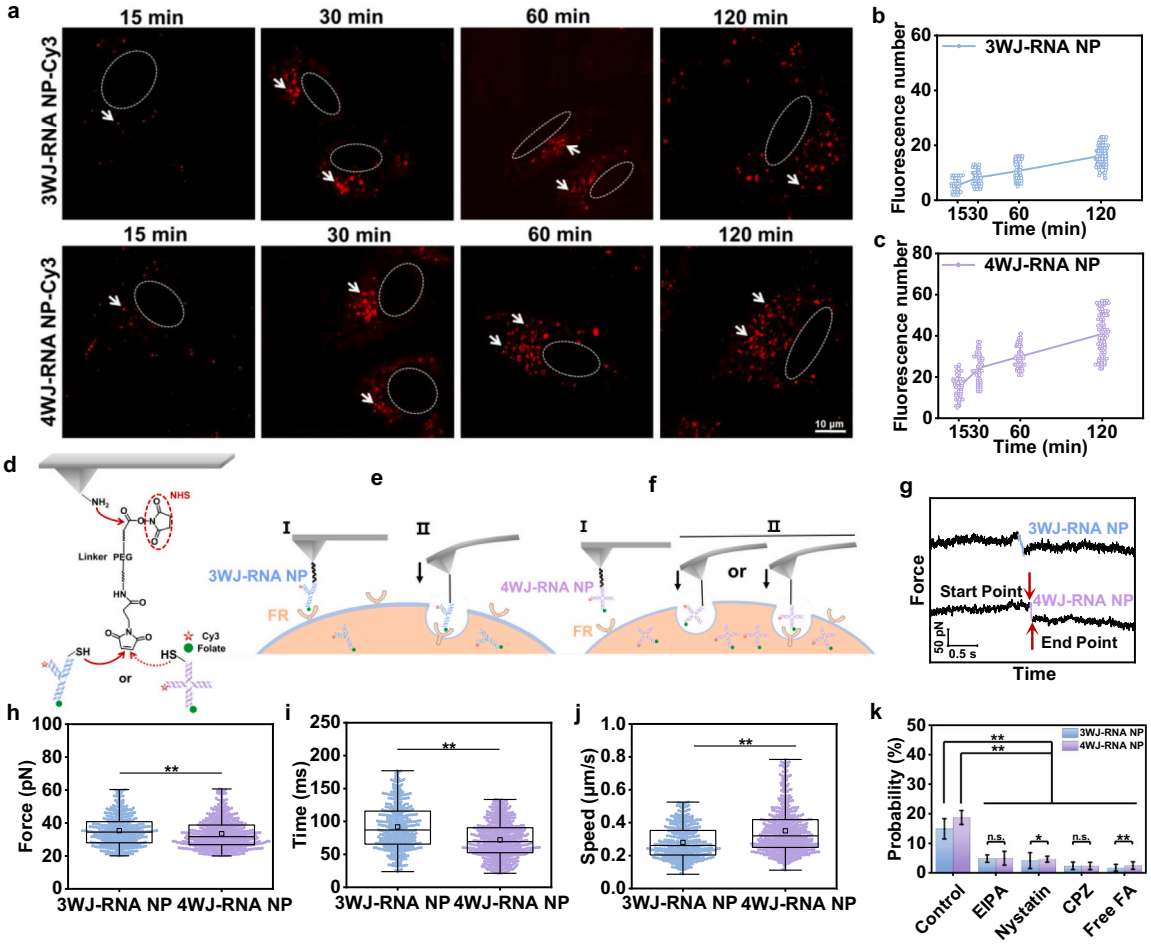

Fig. 1. Investigating the transmembrane transporting of 3WJ-RNA NPs and 4WJ-RNA NPs. (a) Confocal fluorescence images of HeLa cells after incubation with 3WJ-RNA NPs and 4WJ-RNA NPs for different time (15, 30, 60, and 120 min), the white dashed line circle indicates nucleus. (b, c) Dot line chart of fluorescence number for 3WJ-RNA NPs and 4WJ-RNA NPs, the circle represents the fluorescence number in each cell. The results are the mean value from three independent experiments. N ≈ 50. (d) 3WJ-RNA NPs or 4WJ-RNA NPs are attached to the AFM tip via a heterobifunctional PEG linker. (e, f) Schematic diagram for monitoring the cell internalization of 3WJ-RNA NP and 4WJ-RNA NP with force tracing, respectively. (g) The typical force-time curves for single RNA NP entry into cell. (h-j) Boxplot of the distribution of force, time, and speed for RNA NP entry into cell, respectively. N ≈ 450. The box indicates the 25th and 75th percentiles, the square in the box indicates the mean value, the horizontal line in the box indicates the median, and the colored dots indicate each data. (k) Probability of observing the force-time signal for 3WJ-RNA NP and 4WJ-RNA NP entry into cell before and after blocking with EIPA, Nystatin, CPZ, and free FA, respectively. The results are the mean value from three independent experiments. This value is reported as the mean ± standard deviation. *P* value was determined by a two-sample *t*-test, $^{**}P < 0.01$.

3WJ-RNA NP and 4WJ-RNA NP, respectively (Fig. S4b, d). And the corresponding duration ranges from 20 to 175 ms with the mean value of 91 ± 34 ms and 72 ± 27 ms (Fig. S4c, e). The average speed was calculated by displacement/duration, which is 0.28 μm/s and 0.36 μm/s for 3WJ-RNA NP and 4WJ-RNA NP, respectively (Fig. 1j, Fig. S4f, g). It is found that the force required for cellular internalization is nearly identical for 3WJ-RNA NP and 4WJ-RNA NP (Fig. 1h). However, the 4WJ-RNA NP exhibits a shorter transmembrane duration (Fig. 1i) and a faster transmembrane transport speed. Meanwhile, the probability of observing the force-time signals is higher for 4WJ-RNA NP (18.7 %) compared to 3WJ-RNA NP (14.9 %, Fig. 1k). To exclude influence from PEG linker, we conducted force tracing measurements on HeLa cells using AFM tips only modified with PEG linker. It is found that only the fluctuation from cell membrane was measured, with small force value (Fig. S5a, b).

The higher transmembrane transport efficiency of 4WJ-RNA NP may be attributed to its unique "+" shape, which could potentially confer higher motile and deformative properties. We speculate that the 4WJ-RNA NP with more and longer branches, may exhibit a rubber-like deformation property. This property, in theory, would provide more opportunities to interact with the cell membrane and facilitate membrane deformation [30–32]. It is hypothesized that 4WJ-RNA NPs undergo transient structural deformation to traverse the cell membrane, subsequently recovering their native conformation. Additionally, the unmodified vacancy in the 4WJ-C strand is speculated to potentially promote additional non-receptor mediated endocytosis (Fig. 1f). After blocking with free FA (10 μM, 30 min), the probability of observing cell internalization decreased to 1.7 % and 2.4 % for 3WJ-RNA NP and 4WJ-RNA NP, respectively. The slightly higher probability for 4WJ-RNA NP may stem from non-specific binding of the vacancy, promoting additional endocytic uptake. In addition, after inhibition with free FA at 30 μM (30 min), the probability remains similar to that at 10 μM. In contrast, following treatment with free FA at 5 μM (30 min), the probability of 3WJ-RNA NPs and 4WJ-RNA NPs entering cell is 3.5 % and 4.4 % respectively, the results indicate that the internalization rate is slightly affected, and the FR circulation is saturated with 10 μM FA incubation (Fig. S6).

The conclusion was further verified by performing SMFS on cell membrane, which allows quantifying molecular recognition and interaction dynamic features within biological systems at the single molecule level [33–35]. The probability of capturing the force-distance signal for 4WJ-RNA NP binding with cell membrane (45.2 %) is higher than that of

3WJ-RNA NP (39.2 %, Fig. S7d). The higher probability from the nonspecific binding of 4WJ-C strand with cell membrane, as shown in the left part of the dashed line (Fig. S7a-c, e, f). We also conducted SMFS on Vero cell line (normal cell without FR overexpression), the probability of RNA NPs binding to the cell membrane reduces from 39.2 % and 45.2 % to 15.2 % and 15.5 % for 3WJ-RNA NPs and 4WJ-RNA NPs, respectively (Table S1). Furthermore, the probability of observed force-time signal for 3WJ-RNA NP and 4WJ-RNA NP entering Vero cell decreases from 14.9 % and 18.7 % to 4.2 % and 5.3 %, respectively (Table S2). The details of the dynamic parameters are given in Fig. S8 and Table S3.

Elucidating the cell internalization pathway of RNA nano-drugs is key to accelerating their clinical application [29]. Previous reports have suggested that the endocytosis pathway for RNA NPs carrying different ligands may vary and could occur via macropinocytosis, caveolin-mediated endocytosis, or clathrin-mediated endocytosis [36,37]. To explore the pathway of RNA NPs entry into cell, blocking experiments were performed. After blocking with EIPA (5-(N-Ethyl-N isopropyl), amiloride), nystatin, and CPZ (chlorpromazine), the probability of detected force-time signal decreases from 14.9 % to 4.7 %, 4.1 %, and 2.4 %, respectively for 3WJ-RNA NP. For 4WJ-RNA NP, the corresponding probability decreases from 18.7 % to 4.9 %, 4.6 %, and 2.3 %, respectively (Fig. 1k). And the relevant dynamic parameters are identified with that before blocking (Fig. S9a, b).

The confocal fluorescence imaging further confirmed the conclusion (Fig. S10a). The RNA NPs endocytosis is severely impaired with CPZ, many RNA NPs just locates on the cell membrane (Fig. S10b). Furthermore, we visualized the localization of RNA NPs (red) within green

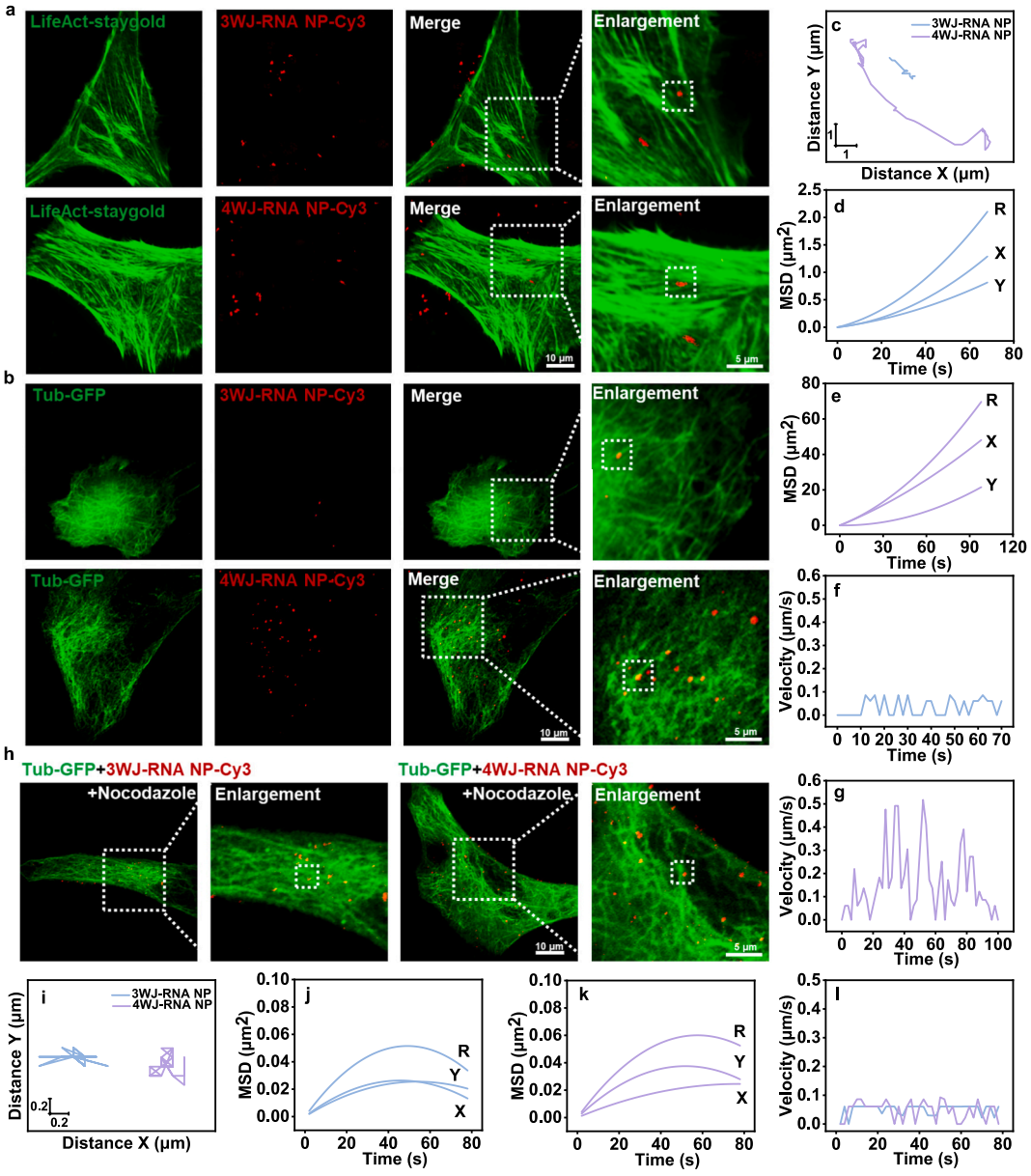

Fig. 2. The intracellular transport of RNA NPs depending on microtubules. (a, b) Fluorescence images of 3WJ-RNA NPs and 4WJ-RNA NPs cocultured cells labeling with actin and microtubule, respectively. (c) Trajectory for 3WJ-RNA NPs and 4WJ-RNA NPs movement along microtubule. (d, e) Typical MSD-$\triangle t$ plots for the 3WJ-RNA NPs and 4WJ-RNA NPs respectively. X, Y, and R indicates diffusion in the X, Y direction and a two-dimensional plane, respectively. (f, g) Analyzing the instantaneous transport velocity of the 3WJ-RNA NPs and 4WJ-RNA NPs, respectively. (h) Fluorescence images of Tub-GFP labeling cells treated with nocodazole and cocultured with 3WJ-RNA NPs/4WJ-RNA NPs. (i) Typical trajectory of 3WJ-RNA NPs and 4WJ-RNA NPs after treating with nocodazole. (j, k) Typical MSD-$\triangle t$ plots for the 3WJ-RNA NPs and 4WJ-RNA NPs respectively. X, Y, and R indicates diffusion in the X, Y direction and a two-dimensional plane, respectively. (l) Analysis the instantaneous transport velocity of the 3WJ-RNA NPs and 4WJ-RNA NPs after treating with nocodazole.

fluorescent protein (GFP)-clathrin coated vesicles (Fig. S10c). Taken together, these results support that the RNA NPs enter cell via macropinocytosis, caveolin-mediated endocytosis, and mainly through clathrin-mediated endocytosis.

3.2. The microtubule-dependent intracellular transporting of RNA NPs

After internalization via transmembrane transporting, the vesicles carrying RNA NPs will start the journey of intracellular delivery. Actin filaments and microtubules are the main components of the cytoskeleton related to intracellular transport [38]. Generally, actin filaments are responsible for movements at the cell periphery area, whereas microtubules are responsible for long-distance transport to the perinuclear region [39]. Herein, dual-color fluorescence images indicate the co-transporting of RNA NPs with microtubules but not actin filaments (Fig. 2a, b). The trajectory analysis reveals the greater displacement of 4WJ-RNA NPs (around 7 μm in X and Y direction) compared to 3WJ-RNA NPs (around 1 μm in X and Y direction, Fig. 2c). Then, MSD analysis of the trajectory was conducted to determine the motion types according to the literature [25], indicating the directed diffusion along microtubules (Fig. 2d, e). The diffusion coefficient (D) is calculated as 8.0×10^{-10} cm^2/s for 4WJ-RNA NPs, which is much larger than that of 3WJ-RNA NPs (2.4×10^{-11} cm^2/s). Meanwhile, the velocity of 4WJ-RNA NPs (0.0005–0.517 μm/s) is relatively faster than that of 3WJ-RNA NPs (0.0003–0.086 μm/s, Fig. 2f, g), these results demonstrate the higher intracellular transporting ability of 4WJ-RNA NPs. To confirm microtubule-dependent RNA NPs transport, we treated cells with nocodazole (30 μM, 30 min) to disrupt the polymerization of microtubules [40]. RNA NPs is trapped in a very small range (around 0.4 μm in X and Y direction for 3WJ-RNA NPs, around 1 μm in X and Y direction for 4WJ-RNA NPs, Fig. 2h, i). According to the MSD-$\triangle t$ plots in the X, Y direction and a two-dimensional plane [41], the both RNA NPs are classified as restricted diffusion mode (Fig. 2j, k). The D for 3WJ-RNA NPs and 4WJ-RNA NPs is 0.53×10^{-11} cm^2/s, which is characterized by notably low motion speed of 0.0001–0.061 μm/s for 3WJ-RNA NPs and 0.0001–0.093 μm/s for 4WJ-RNA NPs (Fig. 2l). Furthermore, the microtubule motor proteins (kinesin) was inhibited, using the inhibitor of monastrol [42]. After inhibition, the both RNA NPs exhibit a restricted diffusion mode (Fig. S11a-d). The D for 3WJ-RNA NPs and 4WJ-RNA NPs is 1.0×10^{-11} cm^2/s and 1.4×10^{-11} cm^2/s, respectively. The corresponding speed of 0.0001–0.0732 μm/s (Fig. S11e) is similar to that inhibited with nocodazole, much slower than that before inhibition. To explicitly rule out the involvement of actin, we treated cells with cytochalasin D to disrupt actin filaments [43], the D is 0.22×10^{-11} cm^2/s and 0.68×10^{-11} cm^2/s for 3WJ-RNA NPs and 4WJ-RNA NPs, respectively, while the speed range remained similar (0.0001–0.0782 μm/s) (Fig. S12). These results suggest that the intracellular transport of RNA NPs relies on microtubules, and the actin filament will also affect. In addition, the cell viability after coincubation with various inhibitors was assessed, the results confirm that the coincubation concentration and time used in the experiments do not cause cytotoxicity (Fig. S13).

3.3. Tracking the cotransport of RNA NPs with endosomes

The RNA NPs enter cell via clathrin-mediated endocytosis forming endocytic vesicles and transport along microtubes, then they are sorted into the endosomes. During the endosomal phase, RNA NPs may undergo several complex delivery pathway until being transported to the lysosomal compartments [44]. Following endocytosis, RNA NPs are typically sequestered in the early endosomes and late endosomes in sequence [45,46]. The fluorescence imaging shows the co-localization of 3WJ-RNA NPs/4WJ-RNA NPs with Rab5-GFP labeled early endosomes (Fig. 3a). Trajectory analysis shows that the motion range of around 0.4 μm in X direction and 1.6 μm in Y direction for 3WJ-RNA NPs, and around 1 μm in X direction and 2 μm in Y direction for 4WJ-RNA NPs (Fig. 3b). Both the 3WJ-RNA NPs and 4WJ-RNA NPs exhibit a directed diffusion mode in early endosomes (Fig. 3c, d) with the transport velocity of 0.0003–0.122 μm/s and 0.0006–0.273 μm/s, respectively (Fig. 3e, f). Subsequently, the RNA NPs will progressively traffic towards the Rab7-GFP labeled late endosomes (Fig. 3g). The 4WJ-RNA NPs still move in a directed diffusion mode, and the trajectory exhibits a linear trend (2 μm in X direction and 6 μm in Y direction) with velocity of 0.0001–0.329 μm/s (Fig. 3h, j, l). However, the 3WJ-RNA NPs exhibit a simple diffusion mode, and the motion range is around1.2 μm in X direction and 2 μm in Y direction with velocity of 0.0001–0.305 μm/s (Fig. 3h, i, k). It is found that whether in early endosomes or late endosomes, the transporting of 4WJ-RNA NPs is faster than that of 3WJ-RNA NPs due to the higher motile and deformative properties. Moreover, the speed in late endosomes is higher than that in early endosomes, which is consistent with previous report [47]. Meanwhile, some of the RNA NPs were observed escaping from early endosomes, the simultaneous snapshots of the vesicles (dashed line circles in Fig. 3m, r) show the process of 3WJ-RNA NPs and 4WJ-RNA NPs escaping from early endosomes with the time scale of ~100 s. As time going, the synergistically transporting is non-apparent, the RNA NPs and early endosomes gradually separate with different velocity (from start point to end point in trajectory, Fig. 3n-q, s-v). However, the escaping of RNA NPs from late endosomes was not observed during the tracking, the RNA NPs and late endosomes always locate together (Fig. S14).

Some of the RNA NPs will transport from early endosomes to recycling endosomes, the fusion of early endosomes with recycling endosomes can direct a few particles towards the plasma membrane [44]. Herein, the co-transporting of Rab11-GFP labeled recycling endosomes and 3WJ-RNA NPs/4WJ-RNA NPs were captured (Fig. S15a). The 3WJ-RNA NPs still exhibit simple diffusion mode with the motion range of around 1 μm in X direction and 1.6 μm in Y direction. Similarly, the 4WJ-RNA NPs maintain directed diffusion mode with the range of around 4 μm in X direction and 1.4 μm in Y direction (Fig. S15b-d). However, they show the similar velocity of 0.0002–0.244 μm/s and 0.0003–0.259 μm/s, respectively (Fig. S15e, f).

Furthermore, some of the RNA NPs will transport from early endosomes and late endosomes to multivesicular bodies [48]. Here, the co-transporting of CD63-GFP labeled multivesicular bodies and 3WJ-RNA NPs/4WJ-RNA NPs was visualized (Fig. 4a). In Y direction, they show the similar motion scale of ~8 μm, the motion range in X direction for 4WJ-RNA NPs is ~2.5 μm, which is fourfold of 3WJ-RNA NPs (~0.6 μm, Fig. 4b). The velocity of 3WJ-RNA NPs and 4WJ-RNA NPs is similar (0.0005–0.371 μm/s and 0.0006–0.329 μm/s, respectively), the 3WJ-RNA NPs still move in simple diffusion mode and the 4WJ-RNA NPs still move in directed diffusion mode (Fig. 4c-e). Additionally, after coincubation for 2 h and 6 h, the colocalization Pearson's R value is indiscriminate (0.212 and 0.281 for 3WJ-RNA NPs, 0.261 and 0.293 for 4WJ-RNA NPs, Fig. 4i) without obvious changing of the mean fluorescence intensity (Fig. 4f-h). The simultaneous snapshots further confirm that RNA NPs cotransport with multivesicular bodies without endosomal escape during tracking time (Fig. 4j, k, Fig. S16).

3.4. Transport of RNA NPs with lysosomes

RNA NPs are taken up into cells via endocytic pathway where they are entrapped in endosomes and finally trafficked into lysosomal compartments [49]. Herein, the co-transporting of Lamp-GFP labeled lysosomes with 3WJ-RNA NPs/4WJ-RNA NPs were observed (Fig. 5a). The representative trajectory (Fig. 5b) analysis reveals that the movement range of 4WJ-RNA NPs (~10 μm in X direction and ~ 8 μm in Y direction) is greater than that of 3WJ-RNA NPs (~1.6 μm in X direction and ~ 1.5 μm in Y direction). Furthermore, the 4WJ-RNA NPs exhibit a linear trajectory, in contrast to the inorganized trajectory of 3WJ-RNA NPs. The 3WJ-RNA NPs move in a restricted diffusion mode with the velocity of 0.008–0.492 μm/s, whereas the 4WJ-RNA NPs still maintain a directed diffusion movement with the higher velocity of 0.012–1.508 μm/s (Fig. 5c-e). Both the 3WJ-RNA NPs and 4WJ-RNA NPs exhibit high

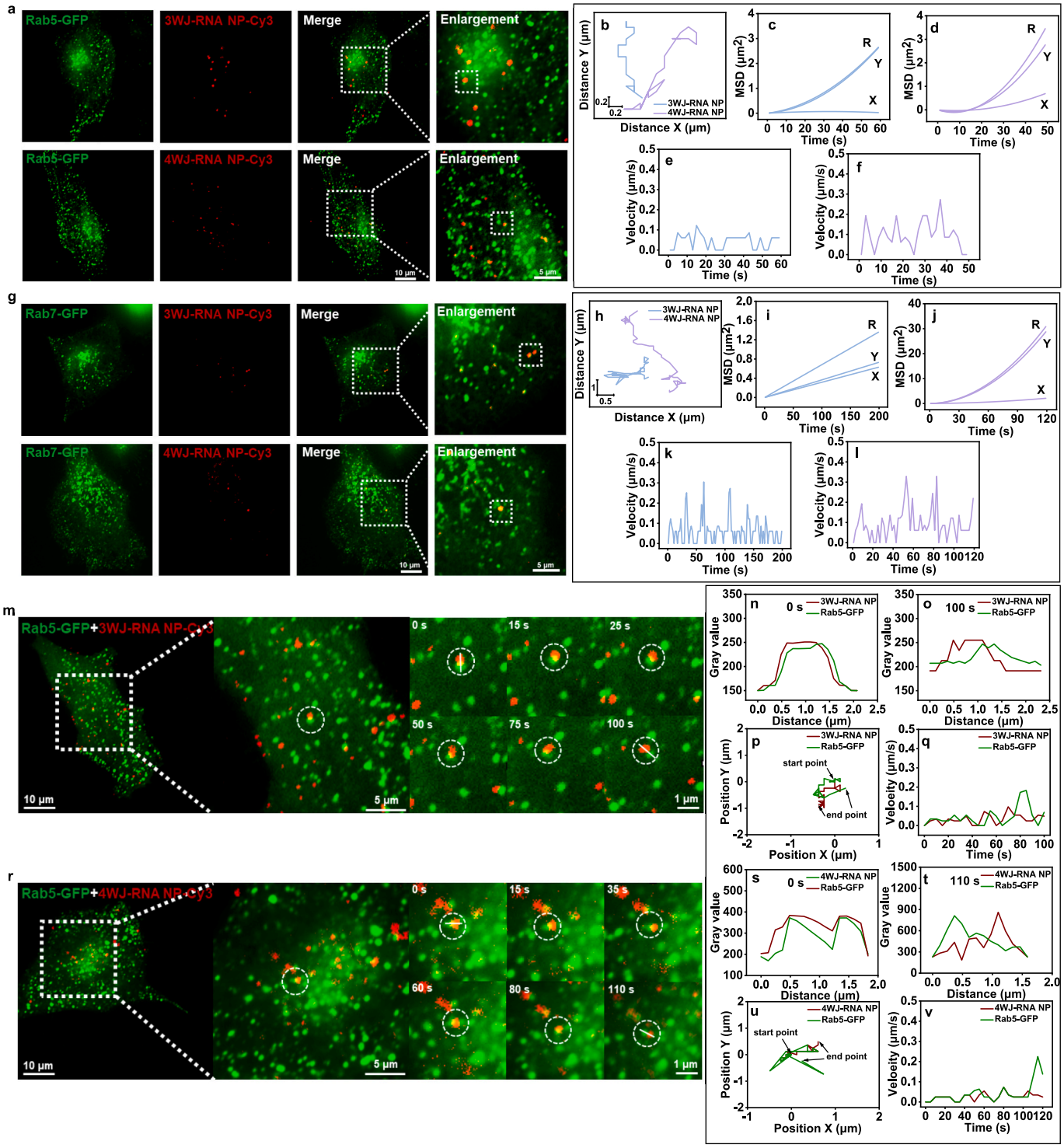

Fig. 3. Transport of RNA NPs with early endosomes and late endosomes. (a) Fluorescence images of 3WJ-RNA NPs/4WJ-RNA NPs co-transporting with early endosomes. (b) Typical trajectory of 3WJ-RNA NPs and 4WJ-RNA NPs co-transporting with early endosomes. (c, d) Typical MSD-$\triangle t$ plots for 3WJ-RNA NPs and 4WJ-RNA NPs, respectively. X, Y, and R indicates diffusion in the X, Y direction and in a two-dimensional plane, respectively. (e, f) The analysis of instantaneous transport velocity for 3WJ-RNA NPs and 4WJ-RNA NPs, respectively. (g) Fluorescence images of 3WJ-RNA NPs/4WJ-RNA NPs co-transporting with late endosomes. (h) Typical trajectory of 3WJ-RNA NPs and 4WJ-RNA NPs co-transported with late endosomes. (i, j) Typical MSD-$\triangle t$ plots for the 3WJ-RNA NPs and 4WJ-RNA NPs, respectively. X, Y, and R indicates diffusion in the X, Y direction and in a two-dimensional plane, respectively. (k, l) The analysis of instantaneous transport velocity for 3WJ-RNA NPs and 4WJ-RNA NPs, respectively. (m) Snapshots of 3WJ-RNA NPs escaping from early endosomes. (n, o) The gray value profile of early endosomes and 3WJ-RNA NPs at 0 s and 100 s (according to white line in m), respectively. (p) The corresponding trajectory of 3WJ-RNA NPs and early endosomes (dashed line circle). (q) The instantaneous velocity analysis of 3WJ-RNA NPs and early endosomes during escaping. (r) Snapshots of 4WJ-RNA NPs escaping from early endosomes. (s, t) The gray value profile of early endosomes and 4WJ-RNA NPs at 0 s and 110 s (according to white line in r), respectively. (u) The corresponding trajectory of 4WJ-RNA NPs and early endosomes (dashed line circle). (v) The instantaneous velocity analysis of 4WJ-RNA NPs and early endosomes during escaping.

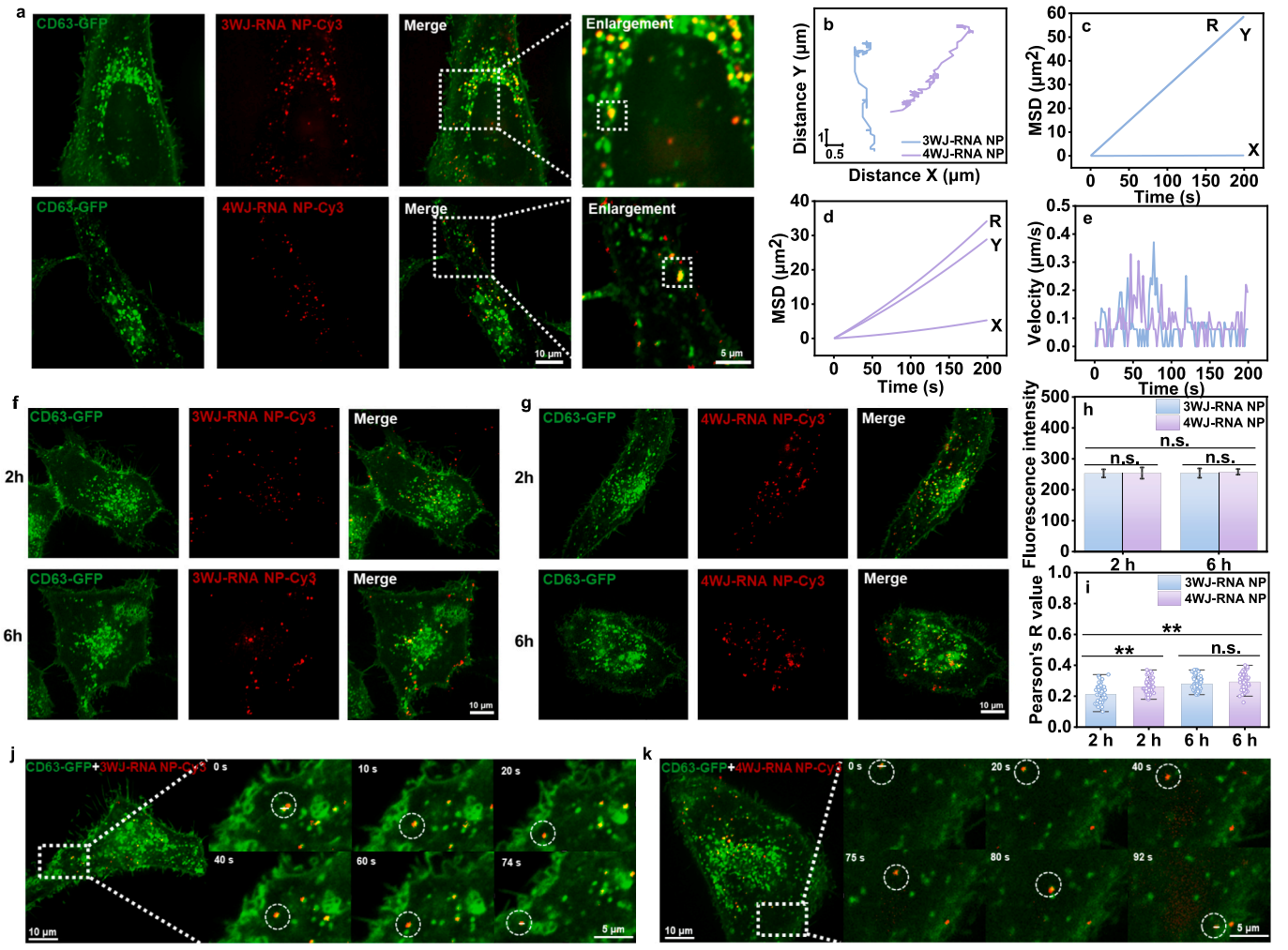

Fig. 4. Transport of RNA NPs with multivesicular bodies. (a) Fluorescence images of 3WJ-RNA NPs/4WJ-RNA NPs co-transporting with multivesicular bodies. (b) Typical trajectory of 3WJ-RNA NPs and 4WJ-RNA NPs co-transporting with multivesicular bodies. (c, d) Typical MSD-$\triangle t$ plots for the 3WJ-RNA NPs and 4WJ-RNA NPs, respectively. X, Y, and R indicates diffusion in the X, Y directions and in a two-dimensional plane, respectively. (e) The analysis of instantaneous transport velocity of the 3WJ-RNA NPs and 4WJ-RNA NPs. (f, g) Fluorescence images of cells transfected with CD63-GFP after incubation with 3WJ-RNA NPs and 4WJ-RNA NPs for different time (2 h and 6 h), respectively. (h) Average fluorescence intensity for 3WJ-RNA NPs and 4WJ-RNA NPs at 2 h and 6 h. (i) The Pearson's R value for 3WJ-RNA NPs and 4WJ-RNA NPs with multivesicular bodies at 2 h and 6 h, R is the correlation coefficient. This value is reported as the mean ± standard deviation, N ≈ 60. *P* value was determined by a two-sample *t*-test, n.s.: no significant, $^{**}P < 0.01$. (j, k) Snapshots of 3WJ-RNA NPs and 4WJ-RNA NPs cotransport with multivesicular bodies, respectively.

transporting speed, suggesting the potential of escaping from lysosomes.

The specific enzymes in acidic environment of lysosomes will lead to significant degradation of the RNA NPs, effectively lysosomal escape of Nano-drugs is key to the therapeutic effects [50,51]. After coculturing cells with the RNA NPs for 2 h, the colocalization of RNA NPs with lysosomes was captured. However, after coincubation for 6 h, most of the RNA NPs escape from the lysosomes and release into the cytoplasm (Fig. 5f, g). The colocalization Pearson's R value for 3WJ-RNA NPs at 2 h and 6 h is 0.317 and 0.197, respectively. For 4WJ-RNA NPs, the Pearson's R value is 0.443 and 0.156, respectively (Fig. 5i). These results indicate that both RNA NPs could achieve lysosomal escape, and the 4WJ-RNA NPs show the higher escape efficiency. The equivalent fluorescence intensity at 2 h and 6 h indicates that the RNA NPs can successfully escape from lysosomes but do not degrade (Fig. 5h). The structural integrity of RNA NPs in lysosomes is verified by assessing the size of RNA NPs after incubation in the simulated enzymatic environment of lysosomes, most 4WJ-RNA NPs keep the original size. A few 3WJ-RNA NPs degrade, suggesting the higher stability of 4WJ-RNA NPs (Fig. S17). Meanwhile, the simultaneous snapshots of the vesicles (dashed line circle in Fig. 5j, o) show the process of RNA NPs escaping from lysosomes. The gray value profile at start (0 s) and end point (80 s and 74 s for 3WJ-RNA NPs and 4WJ-RNA NPs, respectively) demonstrates the separation of the RNA NPs from the lysosomes (Fig. 5k, l, p, q). As time going, the trajectory of RNA NPs and lysosomes gradually separate with the varying velocity (Fig. 5m, n, r, s).

Understanding the cellular transport mechanism of RNA NPs is critical for designing more effective RNA nano-drugs. The ideal RNA NPs should exhibit higher transmembrane efficiency, facilitate the intracellular delivery, and escape from endosomes successfully. It is reported that based on phi 29 pRNA, 3WJ-pRNA, 4WJ-pRNA, and branched hexamers have been built and applied in nanomedicine [52,53]. However, the effect of scaffold shape on the RNA NPs transmembrane transport and intracellular delivery remains unclear, Herein, we found that 4WJ-RNA NPs (10 nm) traverse cell membrane more rapidly than 3WJ-RNA NPs (5 nm). Then, the RNA NPs fuse with clathrin and move along microtubules to the early endosomes with directed diffusion mode. Subsequently, the RNA NPs will traffic towards the late endosomes or multivesicular bodies [54]. Alternatively, the early endosomes serve as sorting hubs that direct the payload to the endoplasmic reticulum (ER), trans-Golgi network, or recycling endosomes [44]. The

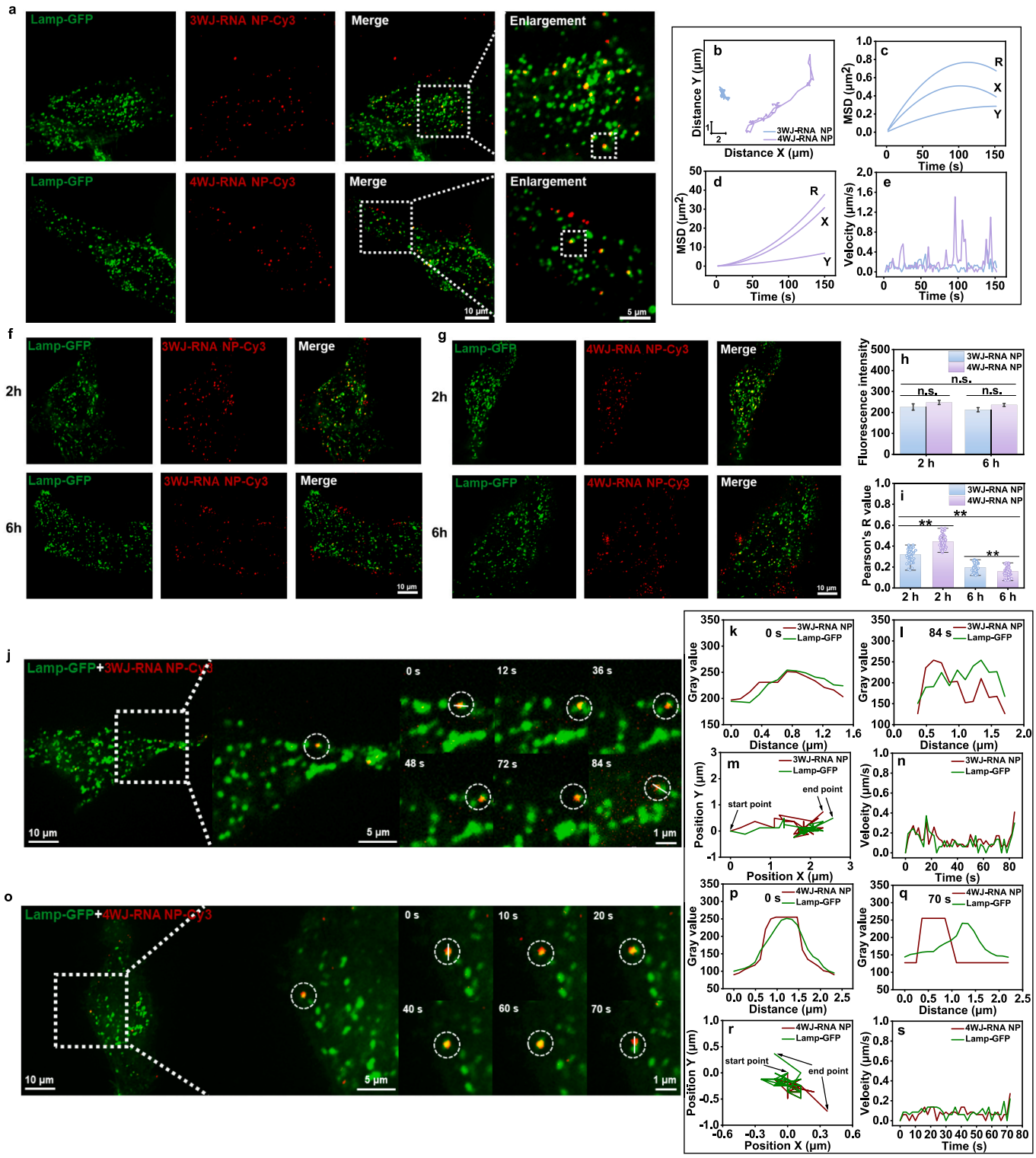

Fig. 5. The co-transporting of RNA NPs with lysosomes. (a) Fluorescence images of 3WJ-RNA NPs/4WJ-RNA NPs localized in lysosomes. (b) The typical trajectory of 3WJ-RNA NPs and 4WJ-RNA NPs co-transport with lysosomes, respectively. (c, d) Typical MSD-$\triangle t$ plots for the 3WJ-RNA NPs and 4WJ-RNA NPs, respectively. X, Y, and R indicates diffusion in the X, Y direction and in a two-dimensional plane, respectively. (e) The analysis of instantaneous transport velocity for the 3WJ-RNA NPs and 4WJ-RNA NPs. (f, g) Fluorescence images of cells transfected with Lamp-GFP after incubation with 3WJ-RNA NPs and 4WJ-RNA NPs for different time (2 h and 6 h), respectively. (h) Average fluorescence intensity for 3WJ-RNA NPs and 4WJ-RNA NPs at 2 h and 6 h. (i) The Pearson's R value for 3WJ-RNA NPs and 4WJ-RNA NPs with lysosomes, R is the correlation coefficient. This value is reported as the mean ± standard deviation, N ≈ 60. *P* value was determined by a two-sample *t*-test, n.s.: no significant, $^{**}P < 0.01$. (j) Snapshots of 3WJ-RNA NPs escaping from lysosomes. (k, l) The gray value profile of lysosomes and 3WJ-RNA NPs at 0 s and 84 s (according to white line in j), respectively. (m) The corresponding trajectory of 3WJ-RNA NPs and lysosomes (dashed line circle). (n) The instantaneous velocity analysis of 3WJ-RNA NPs and lysosomes during escaping. (o) Snapshots of 4WJ-RNA NPs escaping from lysosomes. (p, q) The gray value profile of lysosomes and 4WJ-RNA NPs at 0 s and 70 s (according to white line in o), respectively. (r) The corresponding trajectory of 4WJ-RNA NPs and lysosomes (dashed line circle). (s) The instantaneous transport velocity analysis of 4WJ-RNA NPs and lysosomes during escaping.

recycling endosomes may directly recycle the RNA NPs back to the extracellular environment [55]. We quantified the colocalization fluorescence numbers of RNA NPs with endosomes. In each cell, the fluorescence number for 3WJ-RNA NPs colocalization with clathrin, early endosomes, late endosomes, recycling endosomes, multivesicular bodies, and lysosomes is 12 ± 5, 13 ± 5, 5 ± 2, 6 ± 2, 7 ± 3, and 7 ± 3, respectively. The corresponding number for 4WJ-RNA NPs is 17 ± 6, 11 ± 5, 5 ± 2, 5 ± 2, 8 ± 3, and 7 ± 4, respectively (Fig. 6a). The obvious decreasing in late endosome (vs. early endosomes) suggests their two fates: (1) recycling endosome diversion or (2) early endosome escape. Finally, the RNA NPs will transport to lysosomes via multivesicular bodies or late endosomes, and the colocalization number in multivesicular bodies is a little bit higher than that in late endosomes, indicating the preferable pathway of via multivesicular bodies. The multivesicular bodies pathway may confer dual effects: (i) accelerated lysosomal delivery, yet (ii) potential drug loss via exosomal secretion [56]. The results provide visual evidence for the potential intracellular transport pathway of RNA NPs (Fig. 6b).

The 3WJ-RNA NPs co-transport with late endosomes, recycling endosomes, and multivesicular bodies in simple diffusion mode, even in restricted diffusion mode with lysosomes. However, the 4WJ-RNA NPs consistently move in directed diffusion mode with higher speed, while exhibiting higher endosomal escape efficiency. The longer branched chain of 4WJ-RNA NPs may increase the stability and elasticity and make it more motile [32]. Meanwhile, RNA NPs exhibits more pronounced long-distance intracellular movement, suggesting a preference for unimpeded direction transport within cells.

4. Conclusions

Advances in nanotechnology over the past few decades have enabled the application of RNA NPs in nanomedicine and vaccines. Effective cellular delivery is vital for RNA NPs to exert their therapeutic effects, thorough understanding the cellular delivery dynamic mechanism of RNA NPs can optimize the delivery platforms for nanomedical application. Our findings reveal that the 4WJ-RNA NPs exhibit great transmembrane transport efficiency with higher speed, the 4WJ-RNA NPs also exhibit higher intracellular delivery efficiency with directed diffusion mode. Furthermore, the intracellular transporting pathway of the RNA NPs was identified, the RNA NPs preferentially reaches lysosomes via multivesicular bodies rather than late endosomes. Additionally, the endosomal escape of RNA NPs was observed not only in lysosomes but also in early endosomes, 4WJ-RNA NPs displaying more efficient lysosomal escape. The selection of a more efficient RNA scaffold, such as

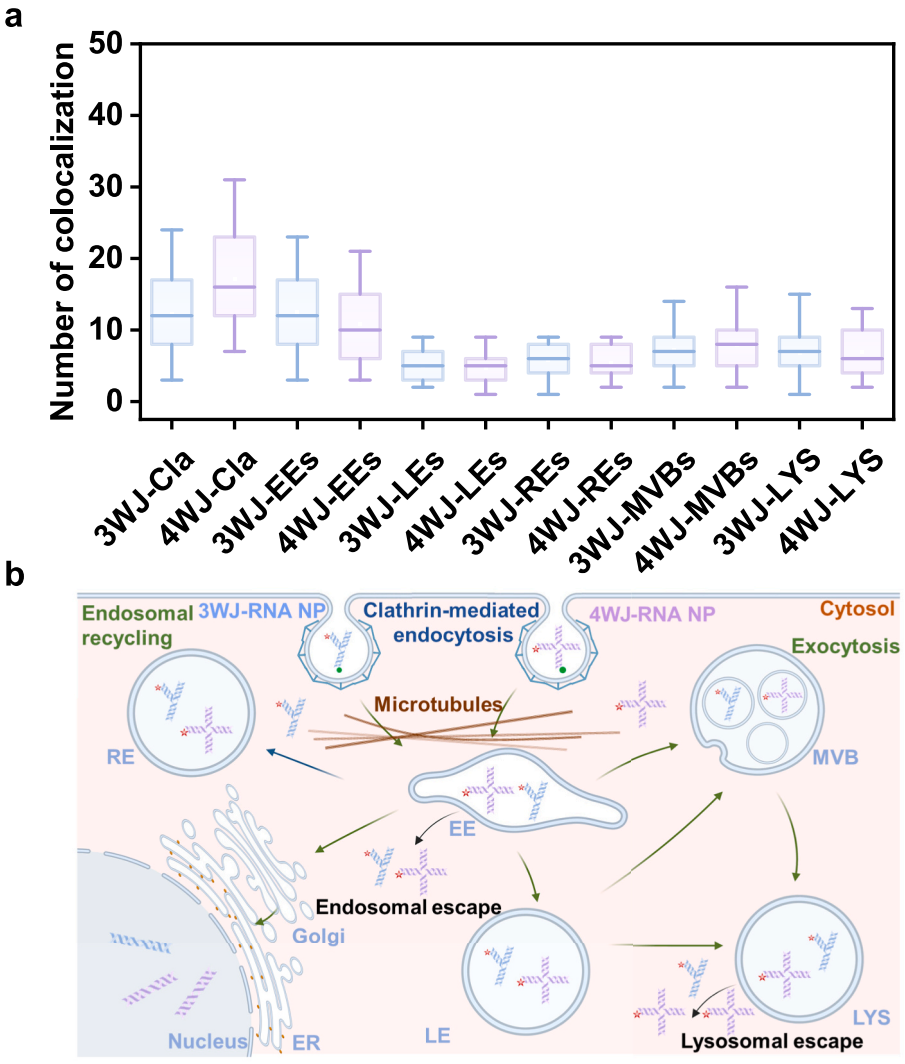

Fig. 6. Intracellular delivery fate of RNA NPs. (a) The colocalization number in each cell for 3WJ-RNA NPs and 4WJ-RNA NPs with clathrin (Cla), early endosomes (EEs), late endosomes (LEs), recycling endosomes (REs), multivesicular bodies (MVBs) and lysosomes (LYS), respectively. The box indicates the 25th and 75th percentiles, the square in the box indicates the mean value, the horizontal line in the box indicates the median. The results are the mean value from three independent experiments. This value is reported as the mean ± standard deviation, N ≈ 80. (b) Schematic of the intracellular delivery pathway of RNA NPs.

4WJ, could potentially reduce drug dosage requirements, improve targeting precision, and enhance the anti-tumor efficacy in the therapeutic application. These findings will offer insights into the development of intelligent diagnostic and therapeutic RNA nanomaterials, facilitating advancements in mRNA vaccines and nanomedicine application.

CRediT authorship contribution statement

Hui Wang: Writing – original draft, Data curation. **Xin Ji:** Methodology. **Haijiao Xu:** Resources. **Siying Li:** Formal analysis. **Hongda Wang:** Funding acquisition. **Yuping Shan:** Writing – review & editing, Methodology, Funding acquisition.

Declaration of competing interest

The authors declare that they have no known competing financial interests or personal relationships that could have appeared to influence the work reported in this paper.

Acknowledgements

This work was supported by Natural Science Foundation of China (Nos. 22377008, 22327808, and 22150003), the Scientific Instrument Developing Project of the Chinese Academy of Sciences (ZDKYYQ20220005), and Jilin Province Science Research Foundation (20250206044ZP).

Appendix A. Supplementary data

Supplementary data to this article can be found online at https://doi.org/10.1016/j.cej.2025.171092.

Data availability

Data will be made available on request.

References

[1] Y. Shu, F. Pi, A. Sharma, M. Rajabi, F. Haque, D. Shu, M. Leggas, B.M. Evers, P. Guo, Stable RNA nanoparticles as potential new generation drugs for cancer therapy, Adv. Drug Deliv. Rev. 66 (2014) 74–89, https://doi.org/10.1016/j.addr.2013.11.006.

[2] P. Guo, The emerging field of RNA nanotechnology, Nat. Nanotechnol. 5 (12) (2010) 833–842, https://doi.org/10.1038/nnano.2010.231.

[3] N. Pardi, M.J. Hogan, F.W. Porter, D. Weissman, mRNA vaccines-a new era in vaccinology, Nat. Rev. Drug Discov. 17 (4) (2018) 261–279, https://doi.org/10.1038/nrd.2017.243.

[4] L. Li, J. Liu, Z. Diao, D. Shu, P. Guo, G. Shen, Evaluation of specific delivery of chimeric Phi29 pRNA/siRNA nanoparticles to multiple tumor cells, Mol. BioSyst. 5 (11) (2009) 1361–1368, https://doi.org/10.1039/b903428e.

[5] P. Tarapore, Y. Shu, P. Guo, S.-M. Ho, Application of Phi29 motor pRNA for targeted therapeutic delivery of siRNA silencing metallothionein-IIA and survivin in ovarian cancers, Mol. Ther. 19 (2) (2011) 386–394, https://doi.org/10.1038/mt.2010.243.

[6] X. Piao, H. Wang, D.W. Binzel, P. Guo, Assessment and comparison of thermal stability of phosphorothioate-DNA, DNA, RNA, 2′-F RNA,and LNA in the context of Phi29 pRNA 3WJ, RNA 24 (1) (2017) 67–76, https://doi.org/10.1261/rna.063057.

[7] B. Zhuo, X. Ou, J. Li, Structure and mechanical stabilities of the three-way junction motifs in prohead RNA, J. Phys. Chem. B 125 (44) (2021) 12125–12134, https://doi.org/10.1021/acs.jpcb.1c04681.

[8] A.C. Hill, S.J. Schroeder, Thermodynamic stabilities of three-way junction nanomotifs in prohead RNA, RNA 23 (4) (2017) 521–529, https://doi.org/10.1261/rna.059220.116.

[9] D.W. Binzel, E. Khisamutdinov, M. Vieweger, J. Ortega, J. Li, P. Guo, Mechanism of three-component collision to produce ultrastable pRNA three-way junction of Phi29 DNA-packaging motor by kinetic assessment, RNA 22 (11) (2016) 1710–1718, https://doi.org/10.1261/rna.057646.116.

[10] D.W. Binzel, X. Li, N. Burns, E. Khan, W.-J. Lee, L.-C. Chen, S. Ellipilli, W. Miles, Y. S. Ho, P. Guo, Thermostability, tunability, and tenacity of RNA as rubbery anionic polymeric materials in nanotechnology and nanomedicine-specific cancer targeting with undetectable toxicity, Chem. Rev. 121 (13) (2021) 7398–7467, https://doi.org/10.1021/acs.chemrev.1c00009.

[11] S. Guo, C. Xu, H. Yin, J. Hill, F. Pi, P. Guo, Tuning the size, shape and structure of RNA nanoparticles for favorable cancer targeting and immunostimulation, Wiley Interdiscip. Rev. Nanomed. Nanobiotechnol. 12 (1) (2019) e1582, https://doi.org/10.1002/wnan.1582.

[12] X. Li, K. Jin, T.-C. Cheng, Y.-C. Liao, W.-J. Lee, A.S. Bhullar, L.-C. Chen, P. Rychahou, M.A. Phelps, Y.S. Ho, P. Guo, RNA four-way junction (4WJ) for spontaneous cancer-targeting, effective tumor-regression, metastasis suppression, fast renal excretion and undetectable toxicity, Biomaterials 305 (2024) 122432, https://doi.org/10.1016/j.biomaterials.2023.122432.

[13] Q. Duan, T. Hu, Q. Zhu, X. Jin, F. Chi, X. Chen, How far are the new wave of mRNA drugs from us? mRNA product current perspective and future development, Front. Immunol. 13 (2022) 974433, https://doi.org/10.3389/fimmu.2022.974433.

[14] Y. Pan, S. Wang, Y. Shan, D. Zhang, J. Gao, M. Zhang, S. Liu, M. Cai, H. Xu, G. Li, Q. Qin, H. Wang, Ultrafast tracking of a single live virion during the invagination of a cell membrane, Small 11 (23) (2015) 2782–2788, https://doi.org/10.1002/smll.201403491.

[15] M. Shan, H. Wang, S. Li, X. Zhang, G. Yang, Y. Shan, Distinguishing the cellular transport of folic acid conjugated nano-drugs among different cell lines by using force tracing technique, Mol. Pharm. 20 (6) (2023) 3234–3240, https://doi.org/10.1021/acs.molpharmaceut.2c01035.

[16] J. Zhao, S. Li, X. Pang, Y. Shan, Evaluating the therapeutic efficacy of nano-drugs targeting epidermal growth factor receptor, Chem. Commun. 58 (16) (2022) 2726–2729, https://doi.org/10.1039/d1cc06754k.

[17] S. Li, R. Wang, J. Li, Y. Liu, Y. Fu, J. Zhou, G. Yang, Y. Shan, Revealing the dynamic mechanism by which transferrin promotes the cellular uptake of HAIYPRH peptide-conjugated nanostructures by force tracing, Mol. Pharm. 18 (3) (2021) 1480–1485, https://doi.org/10.1021/acs.molpharmaceut.0c01119.

[18] X. Zhang, M. Shan, S. Li, J. Zhao, X. Pang, G. Yang, Y. Shan, Investigating the transmembrane transport of HAIYPRH peptide-decorated nano-drugs, Phys. Chem. Chem. Phys. 25 (14) (2023) 9766–9771, https://doi.org/10.1039/d3cp00342f.

[19] B. Yang, H. Xu, S. Wang, M. Cai, Y. Shi, G. Yang, H. Wang, Y. Shan, Studying the dynamic mechanism of transporting a single drug carrier-polyamidoamine dendrimer through cell membranes by force tracing, Nanoscale 8 (42) (2016) 18027–18031, https://doi.org/10.1039/c6nr05838h.

[20] Y. Yang, Q. Zhang, M. Cai, H. Xu, D. Lu, Y. Liu, Y. Fu, G. Yang, Y. Shan, Size-dependent transmembrane transport of gold nanocages, ACS Omega 5 (17) (2020) 9864–9869, https://doi.org/10.1021/acsomega.0c00079.

[21] Y.-F. Wang, Q. Zhang, F. Tian, H. Wang, Y. Wang, X. Ma, Q. Huang, M. Cai, Y. Ji, X. Wu, Y. Gan, Y. Yan, K.A. Dawson, S. Guo, J. Zhang, X. Shi, Y. Shan, X.-J. Liang, Spatiotemporal tracing of the cellular internalization process of rod-shaped nanostructures, ACS Nano 16 (3) (2022) 4059–4071, https://doi.org/10.1021/acsnano.1c09684.

[22] Y. Liu, Y. Yang, Q. Zhang, D. Lu, S. Li, J. Li, G. Yang, Y. Shan, Dynamics of delivering aptamer targeted nano-drugs into cells, J. Mater. Chem. B 9 (4) (2021) 952–957, https://doi.org/10.1039/d0tb02527e.

[23] S. Li, X. Pang, J. Zhao, Q. Zhang, Y. Shan, Evaluating the single-molecule interactions between targeted peptides and the receptors on living cell membrane, Nanoscale 13 (41) (2021) 17318–17324, https://doi.org/10.1039/d1nr05547j.

[24] H. Xu, J. Zhang, Y. Zhou, G. Zhao, M. Cai, J. Gao, L. Shao, Y. Shi, H. Li, H. Ji, Y. Zhao, H. Wang, Mechanistic insights into membrane protein clustering revealed by visualizing EGFR secretion, Research 2022 (2022) 9835035, https://doi.org/10.34133/2022/9835035.

[25] A. Kusumi, Y. Sako, M. Yamamoto, Confined lateral diffusion of membrane receptors as studied by single particle tracking (nanovid microscopy). Effects of calcium-induced differentiation in cultured epithelial cells, Biophys. J. 65 (5) (1993) 2021–2040, https://doi.org/10.1016/s0006-3495(93)81253-0.

[26] L. Wang, Q. Li, X. Wen, X. Zhang, S. Wang, Q. Qin, Dissecting the early and late endosomal pathways of Singapore grouper iridovirus by single-particle tracking in living cells, Int. J. Biol. Macromol. 256 (2024) 128336, https://doi.org/10.1016/j.ijbiomac.2023.128336.

[27] D. Shu, Y. Shu, F. Haque, S. Abdelmawla, P. Guo, Thermodynamically stable RNA three-way junction for constructing multifunctional nanoparticles for delivery of therapeutics, Nat. Nanotechnol. 6 (10) (2011) 658–667, https://doi.org/10.1038/nnano.2011.105.

[28] S. Guo, M. Vieweger, K. Zhang, H. Yin, H. Wang, X. Li, S. Li, S. Hu, A. Sparreboom, B.M. Evers, Y. Dong, W. Chiu, P. Guo, Ultra-thermostable RNA nanoparticles for solubilizing and high-yield loading of paclitaxel for breast cancer therapy, Nat. Commun. 11 (1) (2020), https://doi.org/10.1038/s41467-020-14780-5.

[29] C. Xu, F. Haque, D.L. Jasinski, D.W. Binzel, D. Shu, P. Guo, Favorable biodistribution, specific targeting and conditional endosomal escape of RNA nanoparticles in cancer therapy, Cancer Lett. 414 (2018) 57–70, https://doi.org/10.1016/j.canlet.2017.09.043.

[30] X. Li, A.S. Bhullar, D.W. Binzel, P. Guo, The dynamic, motile and deformative properties of RNA nanoparticles facilitate the third milestone of drug development, Adv. Drug Deliv. Rev. 186 (2022) 114316, https://doi.org/10.1016/j.addr.2022.114316.

[31] C. Ghimire, H. Wang, H. Li, M. Vieweger, C. Xu, P. Guo, RNA nanoparticles as rubber for compelling vessel extravasation to enhance tumor targeting and for fast renal excretion to reduce toxicity, ACS Nano 14 (10) (2020) 13180–13191, https://doi.org/10.1021/acsnano.0c04863.

[32] C. Zhong, Z. Shi, D.W. Binzel, K. Jin, X. Li, P. Guo, S.K. Li, Posterior eye delivery of angiogenesis-inhibiting RNA nanoparticles via subconjunctival injection, Int. J. Pharm. 657 (2024) 124151, https://doi.org/10.1016/j.ijpharm.2024.124151.

[33] Y. Shan, H. Wang, The structure and function of cell membranes examined by atomic force microscopy and single-molecule force spectroscopy, Chem. Soc. Rev. 44 (11) (2015) 3617–3638, https://doi.org/10.1039/c4cs00508b.

[34] Y. Bao, Z. Luo, S. Cui, Environment-dependent single-chain mechanics of synthetic polymers and biomacromolecules by atomic force microscopy-based single-

molecule force spectroscopy and the implications for advanced polymer materials, Chem. Soc. Rev. 49 (9) (2020) 2799–2827, https://doi.org/10.1039/c9cs00855a.
[35] D.J. Müller, A.C. Dumitru, C. Lo Giudice, H.E. Gaub, P. Hinterdorfer, G. Hummer, J.J. De Yoreo, Y.F. Dufrêne, D. Alsteens, Atomic force microscopy-based force spectroscopy and multiparametric imaging of biomolecular and cellular systems, Chem. Rev. 121 (19) (2020) 11701–11725, https://doi.org/10.1021/acs.chemrev.0c00617.
[36] J.J. Rennick, A.P.R. Johnston, R.G. Parton, Key principles and methods for studying the endocytosis of biological and nanoparticle therapeutics, Nat. Nanotechnol. 16 (3) (2021) 266–276, https://doi.org/10.1038/s41565-021-00858-8.
[37] S. Behzadi, V. Serpooshan, W. Tao, M.A. Hamaly, M.Y. Alkawareek, E.C. Dreaden, D. Brown, A.M. Alkilany, O.C. Farokhzad, M. Mahmoudi, Cellular uptake of nanoparticles: journey inside the cell, Chem. Soc. Rev. 46 (14) (2017) 4218–4244, https://doi.org/10.1039/c6cs00636a.
[38] L. Rajendran, H.-J. Knölker, K. Simons, Subcellular targeting strategies for drug design and delivery, Nat. Rev. Drug Discov. 9 (1) (2010) 29–42, https://doi.org/10.1038/nrd2897.
[39] C. Lv, C. Yang, D. Ding, Y. Sun, R. Wang, D. Han, W. Tan, Endocytic pathways and intracellular transport of aptamer-drug conjugates in live cells monitored by single-particle tracking, Anal. Chem. 91 (21) (2019) 13818–13823, https://doi.org/10.1021/acs.analchem.9b03281.
[40] D.C. Guzmán-Ocampo, R. Aguayo-Ortiz, L. Cano-González, R. Castillo, A. Hernández-Campos, L. Dominguez, Effects of the protonation state of titratable residues and the presence of water molecules on nocodazole binding to β-tubulin, ChemMedChem 13 (1) (2017) 20–24, https://doi.org/10.1002/cmdc.201700530.
[41] N. Gal, D. Lechtman-Goldstein, D. Weihs, Particle tracking in living cells: a review of the mean square displacement method and beyond, Rheol. Acta 52 (5) (2013) 425–443, https://doi.org/10.1007/s00397-013-0694-6.
[42] L.A. Marques, S.C. Semprebon, A.M. Niwa, G.F.R. D'Epiro, D. Sartori, Â. de Fátima, L.R. Ribeiro, M.S. Mantovani, Antiproliferative activity of monastrol in human adenocarcinoma (MCF-7) and non-tumor (HB4a) breast cells, Naunyn Schmiedeberg's Arch. Pharmacol. 389 (12) (2016) 1279–1288, https://doi.org/10.1007/s00210-016-1292-9.
[43] K. Shoji, K. Ohashi, K. Sampei, M. Oikawa, K. Mizuno, Cytochalasin D acts as an inhibitor of the actin–cofilin interaction, Biochem. Biophys. Res. Commun. 424 (1) (2012) 52–57, https://doi.org/10.1016/j.bbrc.2012.06.063.
[44] T. Van de Vyver, S.C. De Smedt, K. Raemdonck, Modulating intracellular pathways to improve non-viral delivery of RNA therapeutics, Adv. Drug Deliv. Rev. 181 (2022) 114041, https://doi.org/10.1016/j.addr.2021.114041.
[45] D. Vocelle, O.M. Chesniak, M.R. Smith, C. Chan, S.P. Walton, Kinetic analysis of the intracellular processing of siRNAs by confocal microscopy, Microscopy 69 (6) (2020) 401–407, https://doi.org/10.1093/jmicro/dfaa031.
[46] N. Naslavsky, S. Caplan, The enigmatic endosome–sorting the ins and outs of endocytic trafficking, J. Cell Sci. 131 (13) (2018) jcs216499, https://doi.org/10.1242/jcs.216499.
[47] X. Pang, Q. Zhang, S. Li, J. Zhao, M. Cai, H. Wang, H. Xu, G. Yang, Y. Shan, Spatiotemporal tracking of the transport of RNA nano-drugs: from transmembrane to intracellular delivery, Nanoscale 14 (25) (2022) 8919–8928, https://doi.org/10.1039/d2nr00988a.
[48] C. Menaceur, O. Dusailly, F. Gosselet, L. Fenart, J. Saint-Pol, Vesicular trafficking, a mechanism controlled by cascade activation of rab proteins: focus on Rab27, Biology 12 (12) (2023) 1530, https://doi.org/10.3390/biology12121530.
[49] S. Patel, J. Kim, M. Herrera, A. Mukherjee, A.V. Kabanov, G. Sahay, Brief update on endocytosis of nanomedicines, Adv. Drug Deliv. Rev. 144 (2019) 90–111, https://doi.org/10.1016/j.addr.2019.08.004.
[50] J.A. Mindell, Lysosomal acidification mechanisms, Annu. Rev. Physiol. 74 (1) (2012) 69–86, https://doi.org/10.1146/annurev-physiol-012110-142317.
[51] M. Cai, Y. Yao, D. Yin, R. Zhu, T. Fu, J. Kong, K. Wang, J. Liu, A. Yao, Y. Ruan, W. Shi, Q. Zhu, J. Ni, X. Yin, Enhanced lysosomal escape of cell penetrating peptide-functionalized metal–organic frameworks for co-delivery of survivin siRNA and oridonin, J. Colloid Interface Sci. 646 (2023) 370–380, https://doi.org/10.1016/j.jcis.2023.04.126.
[52] D. Jasinski, F. Haque, D.W. Binzel, P. Guo, Advancement of the emerging field of RNA nanotechnology, ACS Nano 11 (2) (2017) 1142–1164, https://doi.org/10.1021/acsnano.6b05737.
[53] Y. Shu, D. Shu, F. Haque, P. Guo, Fabrication of pRNA nanoparticles to deliver therapeutic RNAs and bioactive compounds into tumor cells, Nat. Protoc. 8 (9) (2013) 1635–1659, https://doi.org/10.1038/nprot.2013.097.
[54] M. Gireud-Goss, S. Reyes, M. Wilson, M. Farley, K. Memarzadeh, S. Srinivasan, N. Sirisaengtaksin, S. Yamashita, S. Tsunoda, F.F. Lang, M.N. Waxham, A.J. Bean, Distinct mechanisms enable inward or outward budding from late endosomes/multivesicular bodies, Exp. Cell Res. 372 (1) (2018) 1–15, https://doi.org/10.1016/j.yexcr.2018.08.027.
[55] F. Joris, S.C. De Smedt, K. Raemdonck, Small molecules convey big messages: boosting non-viral nucleic acid delivery with low molecular weight drugs, Nano Today 16 (2017) 14–29, https://doi.org/10.1016/j.nantod.2017.06.012.
[56] Y. Wang, S. Yuan, L. Zhou, K. Yang, Z. Jin, A. Lin, C. Yang, W. Tian, Cutting-edge progress in the acquisition, modification and therapeutic applications of exosomes for drug delivery, Int. J. Nanomedicine 20 (2025) 5059–5080, https://doi.org/10.2147/ijn.S516840.